IEEE Access
Multidisciplinary | Rapid Review | Open Access Journal

Received 10 September 2022, accepted 26 September 2022, date of publication 5 October 2022, date of current version 14 October 2022.

Digital Object Identifier 10.1109/ACCESS.2022.3212538

RESEARCH ARTICLE

Signal Enhancement in Defect Detection of CFRP Material Using a Combination of Difference of Gaussian Convolutions and Sparse Principal Component Thermography

WEI LIU[1], BEIPING HOU[1], YUAN YAO[2], (Member, IEEE), AND LE ZHOU[1], (Member, IEEE)
[1]School of Automation and Electrical Engineering, Zhejiang University of Science & Technology, Hangzhou, Zhejiang 310023, China
[2]Department of Chemical Engineering, National Tsing Hua University, Hsinchu 30013, Taiwan

Corresponding author: Le Zhou (zhoule@zust.edu.cn)

This work was supported in part by the National Natural Science Foundation of China under Grant 62173306, and in part by the Educational Commission Research Program of Zhejiang Province under Grant Y202044842.

ABSTRACT Owing to its advantages of low-cost and fast detection, pulsed thermography has become a promising technique to detect subsurface defects in materials of carbon fiber reinforced polymer (CFRP). Since defect signals in the detected results always suffer from low contrast due to the instability of detecting environment, feature extraction methods are required to enhance the visualization of defects. However, many state-of-the-art feature extraction methods have difficulties in overcoming the interference from noise and background, so that their effects are limited in highlighting the defects. To solve this problem, a novel methodology of combining signal filtering with feature extraction is proposed in this paper. In this approach, thermal images are first smoothed by a difference of Gaussian convolutional (DoGC) filters, which is designed to eliminate noise and uneven background based on their frequencies. Furthermore, the method of sparse principal component thermography (SPCT) is adopted to extract the features of defects. Two experiments on sample laminates have suggested that, DoGC-SPCT is superior to other feature extraction methods in the following aspects. Firstly, the DoGC filter can effectively eliminate most of the interference, thus facilitating defect identification during the process of feature extraction. Secondly, the computational outcomes show that DoGC-SPCT leads to higher values in the index of signal to noise ratios for the defects. Finally, DoGC-SPCT leads to higher interpretability, which has smoother background in the obtained results.

INDEX TERMS Carbon fiber reinforced polymer, Gaussian convolution, pulsed thermography, subsurface defect, sparse principal component thermography.

I. INTRODUCTION

Carbon fiber reinforced polymer (CFRP) is a kind of advanced composite materials that reveals dominant properties of high mechanical strength, high toughness and resistance to high-temperature [1]. Benefiting from those properties, CFRP has shown its promising applications in industries such as aerospace, automotive and sports [2], [3]. However, external impacts from industrial machinery during the manufacturing process may lead to subsurface defects inside the materials, such as folding, adulteration and fiber breakage [4], [5]. As a negative result, total structure of CFRP will be destroyed under the influence of those defects, and strength or stiffness of the products will no longer be guaranteed. Thus, inspection of materials with respect to the possible presence of subsurface defects is crucially significant to the industrialization of CFRP. On the other hand, since subsurface defects are barely visible from the appearance, non-destructive testing (NDT) techniques are necessary to achieve this goal.

Without harming the tested object, NDT can assess the quality of CFRP through the discontinuities in the

The associate editor coordinating the review of this manuscript and approving it for publication was Ravibabu Mulaveesala.

propagation of heat, sound and electromagnetic wave. For example, Li [6] applied microwave testing for thickness measurement of dielectric coatings on CFRP plates, and achieved high accuracy in situations with both thick and thin coatings. Elena [7] adopted X-ray computed tomography to evaluate the structure of CFRP, and proved that it can offer high resolution detecting results. Salski [8] performed radio-frequency inductive testing on the health monitoring of CFRP. And they exemplified that, this technique allows speeding up of the measurement. Dattoma [9] presented preliminary ultrasonic study on detecting CFRP materials, and showed that ultrasonic scanning is suitable for detection of internal defects in composite materials. Meanwhile, Toyama [10] proposed an ultrasonic inspection for detecting disbands in CFRP based on pulsed laser. Ahmed [11] presented a review in the field of eddy-current testing, and made study on how probe structure factors influenced the accuracy of detecting. However, compared to the techniques above, testing by pulsed thermography (PT) [12] has the advantages of relatively simple setup and fast inspection on large areas, so that it shows great potential as an effective tool for real time monitoring of CFRP production.

During the conduction of PT, the object under examination is stimulated with a short high-powered thermal pulse. Then the heat absorbed by surface of the material will diffuse into the object uniformly before reaching the discontinuous areas. During the cooling process, a sequence of thermograms is obtained to characterize the variation of heat distributions on the surface of the material. Associated with this process are the transient heating of thermal pulse and the instability of detecting environment, and they will bring non-uniform background [13] as well as measurement noise [14], [15] to the informative signals in an additional way. Practically, due to those interference, visibility of the defects inside the original thermogram cannot be ensured.

To enhance thermal contrasts for the defects, one popular idea is to extract features from the original thermographic dataset [16], [17], [18], [19], [20], [21]. Meanwhile, the features can also be utilized to characterize shapes or depths of the defects in an end-to-end way [22], [23], [24]. Many feature extraction methods have been proposed. For instance, Shepard [25] developed the method of thermographic sequence reconstruction, in which thermographic data is decomposed based on the temporal evolution model of thermogram. Another strategy is the pulsed phase thermographic technique [26], whose decomposition is built on the basis of oscillatory functions. Alvarez [27] proposed the method of orthogonal polynomial decomposition, and realized identification of defects as well as estimation of their depths. On the other hand, the method of principal component thermography (PCT) [28] was proposed to achieve compression based on the statistical characteristics of thermographic data. And owing to its flexibility, PCT has become the basic framework for many extensive feature extraction algorithms. One of the newly-developed methods is sparse principal component thermography (SPCT) [29], which allows reduction of noise during the feature extraction and further increases the interpretability of the results. Furthermore, some improvements are also established based on PCT and SPCT. For example, Liu [30] developed the generative principal component thermography, in which samples are augmented by a generative adversarial network (GAN) before the conduction of PCT. In our previous work [31], a method of sparse structural principal component thermography is proposed that augments the original thermographic matrix with shift sampling.

The feature extraction methods above have been proved effective in characterizing defects. However, many issues are still in need of investigation. One of them is that most of the state-of-the-art algorithms have difficulties in distinguishing defect signals from uneven background and measurement noise. Consequently, features of the interference may be mistakenly extracted in these methods. Aiming at the problem above, this paper focuses on the further research of increasing accuracy of the feature extraction methods.

The difficulties above motivate the proposal of alternative techniques that pay more attention to eliminate the interference from the informative signals. According to the literatures, some algorithms have been proposed to subtract undesired signals. In general, they can be categorized as schemes of filtering and factor analysis. With respect to filtering, an approximation of a defect-free thermogram is produced by smoothing the image. In this way, an optimal filter should mask the presence of the defects. Some typical filters are based on median kernel [13] or Gaussian kernel. For example, Grys [32] applied the Gaussian filter to subtract uneven illumination from thermal images, and proposed filtered contrast based on the filtering result. For instance, Zhang [15] proposed a spatial-temporal denoised thermal source separation (STDTSS) method that denoised the thermograms based on a combination of Gaussian filter and Savitzky-Golay filter. As for schemes of factor analysis, thermographic data is modeled as weighted sums of different components, namely non-uniform background and defect signals. Different algorithms are proposed to decompose signals. For instance, Zheng [33] adopted penalized least squares to eliminate noise as well as non-uniform background from the original thermogram. On the other hand, inspired by the idea of blind source separation, Liu [34] employed the independent component analysis to decompose the thermographic data into several independent signals. Meanwhile, other methods can be applied to separate compound signals. For example, Wang [35] applied non-negative matrix factorization to extract compound fault features of bearing. Esteki [36] adopted the method of Fisher linear discriminant analysis to separate spectroscopic signals for food quality assessment.

As a comparison of the schemes above, the methods of filtering can directly estimate the patterns of the interference from each thermogram separately, so that they can be more flexible than those of factor analysis in thermographic denoising. Motivated by the filtering algorithms above, a novel scheme of feature extraction that is a combination of

difference of Gaussian convolutions (DoGC) and SPCT is developed in this paper. In this method, a DoGC filter is developed to eliminate noise and non-uniform background by means of low-pass Gaussian spatial filtering, leaving informative signals for the defects in the filtering result. Furthermore, SPCT is conducted to extract features of the defects, considering the dynamic variation of the temperature on each pixel. Benefit from the filtering process of DoGC, the proposed scheme has potential in overcoming the interference, and it is able to capture the features of the defects more accurately.

The remaining contents of this paper are structured as follows. In Section 2, a PT inspection system is established for acquisition of thermographic data. In Section 3, the methodology of DoGC-SPCT is presented in a detailed manner. Section 4 is devoted to the evaluation of the proposed method for defect enhancement in the experiment. Finally, this paper is ended by reaching some conclusions in Section 5.

A shorter version of this paper has been accepted in the 3rd International Conference on Industrial Artificial Intelligence (IAI 2021) [37]. Compared to our initial conference paper, this manuscript performed more detailed discussion about the theoretical principle of this method. Meanwhile, more experiments were performed in this manuscript to validate the feasibility of this method.

II. PT INSPECTION SYSTEM

The structure of PT inspection system is shown in Fig.1. During the conduction of PT, a light source is applied to generate a short high-powered thermal pulse to stimulate the target. As heat diffuses into the object, an infrared camera is employed to capture the temperature distribution on the surface of the object. Since the whole PT process lasts for quite a short time, the facilities in the system can be connected to a computer to keep in synchronization. Generally, the detected temperature for each pixel of the surface can be represented by a specified color, such that the temperature distribution for the whole surface forms one thermal image.

The sequence of thermal images captured by PT is shown on the right side of Fig.1, which can be viewed as a three-dimensional (3D) matrix. The thermographic matrix has dimensionality of $N_y \times N_x \times N_t$, where N_t is the number of frames obtained by the camera, while N_x and N_y are the numbers of pixels in the horizontal and vertical directions respectively. The value of N_t is decided by both the duration of the process and the shooting frequency of the camera, while those of N_x and N_y are determined by the resolution of the camera. In the two-dimensional (2D) plane of an image, any one of the pixels can be located as a coordinate point of (x, y) $(x = 1, \ldots, N_x, y = 1, \ldots, N_y)$

III. METHODOLOGY OF DoGC-SPCT

The proposed DoGC-SPCT method aims at increasing the accuracy of the feature extraction with respect to enhancing visualization of defects. There are a total of two stages in this method: signal filtering and feature extraction. The section below will describe the whole pipeline of this methodology, including the analytical model for thermographic signals, DoGC filtering to subtract noise and background, and SPCT to extract features of the defects.

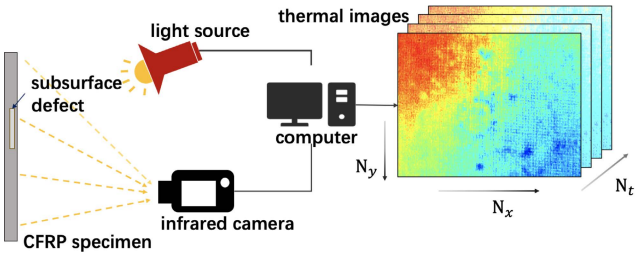

FIGURE 1. Structure of PT for defect detection in CFRP specimen and the captured thermal images.

A. MODEL FOUNDATION

The process of heat diffusion through a solid specimen can be described by Fourier's law [38], given as

$$\frac{\partial}{\partial x}\left(\frac{\partial T}{\partial x}\right)+\frac{\partial}{\partial y}\left(\frac{\partial T}{\partial y}\right)+\frac{\partial}{\partial z}\left(\frac{\partial T}{\partial z}\right)=\frac{1}{\alpha}\left(\frac{\partial T}{\partial t}\right) \quad (1)$$

Here, T is the temperature inside the specimen, which is related to the dimensions of x, y, z and t. α is the thermal diffusivity of the material. After receiving a Dirac heat pulse, the one-dimension (1D) analytical solution of the temperature on the surface of an adiabatic semi-infinite body is given by [19]

$$\mathrm{T}\,(\mathrm{x},\mathrm{y},\mathrm{t}) = T_0 + \mathrm{Q}\,(\mathrm{x},\mathrm{y})\,/(\alpha\sqrt{\pi t}) \quad (2)$$

where T (x, y, t) represents the surface temperature of pixel (x, y) at time t. And T_0 is the initial temperature of the specimen that equals to the ambient environment. Since specimen is kept in a stationary state before being stimulated by the light source, T_0 for each pixel keeps the same in this case. Q(x, y) is the input energy per unit area. Because of non-uniform heating, Q varies at different pixels.

From (2), it can be concluded that, at any moment t, the distribution of the temperature mainly depends on the energy initially stimulated on the specimen. To keep the scale of the temperature, (2) is normalized as follows

$$T_{t,max} = T_0 + Q_{max}/(\alpha\sqrt{\pi t}) \quad (3)$$

$$T_{t,min} = T_0 + Q_{min}/(\alpha\sqrt{\pi t}) \quad (4)$$

$$\Rightarrow \frac{\mathrm{T}(\mathrm{x},\mathrm{y},\mathrm{t})}{T_{t,max}-T_{t,min}} = \frac{T_0\alpha\sqrt{\pi t}}{Q_{max}-Q_{min}} + \frac{\mathrm{Q}(\mathrm{x},\mathrm{y})}{Q_{max}-Q_{min}} \quad (5)$$

where $\frac{\mathrm{T}(\mathrm{x},\mathrm{y},\mathrm{t})}{T_{t,max}-T_{t,min}}$ is the normalized form for each thermogram. Meanwhile, considering the detecting noise $\mathrm{I_n}$ (x, y, t), (5) can be formulated as:

$$\frac{\mathrm{T}(\mathrm{x},\mathrm{y},\mathrm{t})}{T_{t,max}-T_{t,min}} = \frac{T_0\alpha\sqrt{\pi t}}{Q_{max}-Q_{min}} + \frac{\mathrm{Q}(\mathrm{x},\mathrm{y})}{Q_{max}-Q_{min}} + \mathrm{I_n}\,(\mathrm{x},\mathrm{y},\mathrm{t}) \quad (6)$$

The terms in (6) can be replaced as

$$\mathrm{I_m}\,(\mathrm{x},\mathrm{y},\mathrm{t}) = \mathrm{T}(\mathrm{x},\mathrm{y},\mathrm{t})/(T_{t,max}-T_{t,min}) \quad (7)$$

$$\mathrm{I_u}\,(\mathrm{x},\,\mathrm{y}) = \mathrm{Q}(\mathrm{x},\,\mathrm{y})/(Q_{max} - Q_{min}) \tag{8}$$

$$\mathrm{I_i}\,(\mathrm{x},\,\mathrm{y},\,\mathrm{t}) = T_0\alpha\sqrt{\pi t}/(Q_{max} - Q_{min}) \tag{9}$$

Therefore, (6) can be rewritten as

$$\mathrm{I_m}\,(\mathrm{x},\,\mathrm{y},\,\mathrm{t}) = \mathrm{I_i}\,(\mathrm{x},\,\mathrm{y},\,\mathrm{t}) + \mathrm{I_u}\,(\mathrm{x},\,\mathrm{y}) + \mathrm{I_n}\,(\mathrm{x},\,\mathrm{y},\,\mathrm{t}) \tag{10}$$

During the cooling process, if there are no defects inside the material, values of α will keep constant, and I_i will increase uniformly as 1/2 order of time. On the contrary, the internal discontinuities will lead to variation of α, resulting in distinct temporal behavior of the defective pixels. Therefore, from the temporal variation of I_i, it is possible for the feature extracting methods to extract defective pixels that have different time evolution profiles from those intact ones. However, the other terms of $\mathrm{I_u}\,(\mathrm{x},\,\mathrm{y})$ and $\mathrm{I_n}\,(\mathrm{x},\,\mathrm{y},\,\mathrm{t})$ will heavily mask the informative signals. On one hand, I_n corresponds to the random disturbances caused by instability of the detection facility. On the other hand, I_u is related to the distribution of the initial energy, so that signals of I_u correspond to the nonhomogeneous background. These two signals have no connection with the internal defects and make it more difficult to extract features of the defects. For the reasons above, it is necessary to eliminate the signals of I_u and I_n before feature extraction.

In this paper, DoGC filter is proposed to reconstruct the images with least influence of non-uniform background and noise. Fig.2 shows one sampled thermal image recorded by PT inspection, which is demonstrated in a 3D version. The same with [39], in one thermogram, random noise typically consists of sharp transitions in intensity, while signals of uneven background change much more slowly. Besides, the defect signals can be visualized as raised bumps inside the variation of the background. As a conclusion, the general distribution of different frequencies can be described as follows, noise signals are of the highest frequency, followed by that of the defect component, and the frequency of uneven background is the lowest among them.

B. ALGORITHM DESIGN OF DoGC

The main novelty of the proposed methodology lies in the development of DoGC filter, which is able to reduce the noise I_n and non-uniform background I_u in succession. As shown in Fig.3, the DoGC filter is made up of two 2D Gaussian convolutional filters with different filtering thresholds. The section below will introduce the principle of Gaussian convolution as well as the implementation of DoGC filter.

1) 2D GAUSSIAN CONVOLUTION

2D Gaussian convolution is a lowpass spatial domain filter, which performs data smoothing with a kernel sliding over the image. A Gaussian kernel is a rectangular window with a size of $m \times n$, and values of the convolutional coefficients follow the function as below [40]

$$G\,(x,\,y) = \frac{1}{2\pi\sigma^2} exp\left\{-\left[(x - x_0)^2 + (y - y_0)^2\right]/2\sigma^2\right\} \tag{11}$$

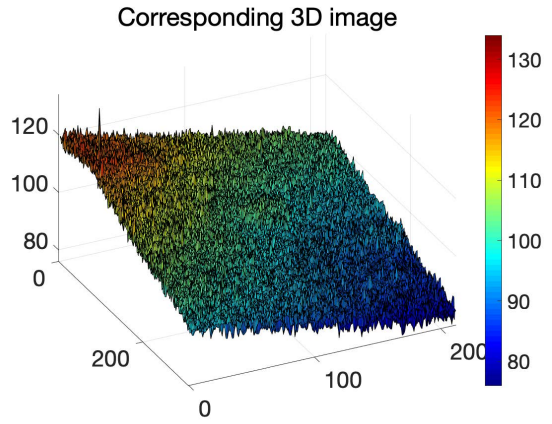

FIGURE 2. The 3D version of one sampled thermal image.

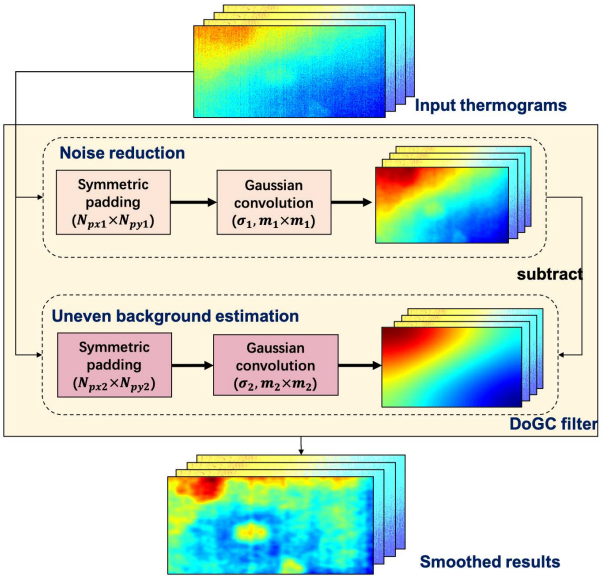

FIGURE 3. Pipeline of the DoGC filter.

where $G\,(x, y)$ is the convolutional coefficient for a pixel (x, y) that is within the scope. Meanwhile, (x_0, y_0) is the current central point when the kernel slides over the whole image. As a rule, both m and n are set as odd integers, such that there is only one central point. From (11), values of $\mathrm{G}\,(\mathrm{x},\,\mathrm{y})$ are subject to a 2D Gaussian distribution, and σ is the standard deviation of the coefficients

The principle of Gaussian convolution is to replace the value of the pixel with a linear combination of its neighborhood. Inside a thermal image, the convolutional operation on I_m can be expressed as

$$I_m * G = \sum_{j=-\left\lceil\frac{n-1}{2}\right\rceil}^{\left\lceil\frac{n-1}{2}\right\rceil} \sum_{i=-\left\lceil\frac{m-1}{2}\right\rceil}^{\left\lceil\frac{m-1}{2}\right\rceil} I_m\,(x+i,\,y+j) \cdot G\,(x+i,\,y+j) \tag{12}$$

where $\lceil a \rceil$ represents the round-up integer of a, and $\mathrm{G(x + i,\,y + j)}$ is the coefficient of pixel $(x + i, y + j)$ inside the kernel centering on (x, y).

2) THE DoGC FILTER

The DoGC filter consists of two Gaussian convolutional filters, which can be described as

$$DoGC(x, y) = I_m(x, y) * G_1 - I_m(x, y) * G_2 \quad (13)$$

where G_1 and G_2 are two Gaussian kernels with different parameters. In this filter, a high cut-off frequency is achieved in $\mathrm{I_m}(x, y) * G_1$, for the purpose of subtracting noise component. While $\mathrm{I_m}(x, y) * G_2$ aims at estimating the underlying shading patterns of the image with a low cut-off frequency. Then, according to (13), the DoGC filter is able to reduce the influence of noise I_n and non-uniform background I_u in sequence.

To achieve this purpose, parameters in the DoGC filter need to be assigned with appropriate values. There are two types of parameters in each kernel, one of them is the kernel size $m \times n$, and the other one is the standard deviation σ. For simplification, square kernels with $m = n$ are applied in this paper. And the values of m are set as the smallest odd integers no less than $\lceil 6\sigma \rceil$, for coefficients at a distance larger than 3σ from the center are small enough to be ignored. As a conclusion, the key parameters that need justifying are σ_1 and σ_2 for G_1 and G_2.

As a low-pass filter, convolution with a Gaussian kernel will reduce irrelevant details in those pixel regions that are small with respect to the size of the filter kernel. In this way, the cut-off frequency of the filter is related to the size of the kernel. Practically, with a larger kernel, more pixels will be taken into account in the smoothing process, and it will lead to a more aggressive blurring. Based on the criteria above, a high cut-off frequency should be achieved in $\mathrm{I_m}(x, y) * G_1$, and a small kernel is needed so as to keep defective information. Accordingly, the value of σ_1 is determined as 3 in this case, so the size of the kernel is equaling to 19×19. On the other hand, the second term $\mathrm{I_m}(x, y) * G_2$ in the filter is to approximate the underlying uneven background. Thus, the parameters in G_2 should be large enough to exclude local information in the result. However, a kernel with a too large size may lead to distortion of the background, so the values of the parameters are determined mainly based on the size of the image. According to the priori research [41], a filtering kernel with the same size as the original image ($N_x \times N_x$ or $N_y \times N_y$) is sufficient for extracting underlying pattern. As a conclusion, the parameters in the DoGC filter are justified in Table 1.

In addition, there is a shrinkage to the size of the image during the process of convolution. Therefore, expanding of the original image is necessary to get a filtered image with the same size as the original one. Considering to keep the continuity for the pattern of the image, symmetric padding [42] is applied in this paper. To guarantee consistency for the sizes of the convolutional results, the size $N_{px} \times N_{py}$ of the padding image can be calculated as

$$N_{px} = N_x + m - 1 \quad (14)$$

$$N_{py} = N_y + n - 1 \quad (15)$$

TABLE 1. Parameters adjustment for the DoGC filter.

	Size of original thermogram	Kernel	σ	m × m
General cases	$N_x \times N_y$	G_1	3	19×19
		G_2	$\begin{cases} \lfloor \frac{N_x}{6} \rfloor & (N_x \le N_y) \\ \lfloor \frac{N_y}{6} \rfloor & (N_y \le N_x) \end{cases}$	$(6\sigma + 1) \times (6\sigma + 1)$
Case 1	308*212	G_1	3	19×19
		G_2	35	211×211
Case 2	270×360	G_1	3	19×19
		G_2	45	271×271

C. FEATURE EXTRACTION

SPCT is applied for a further feature extraction, taking account of the temporal variations of each pixel in the filtered thermograms. Before the conduction of SPCT, a characteristic matrix $\mathbf{X}$ needs to be constructed by converting each image into a vector with a length of N_xN_y. This procedure of vectorization can be implemented row-wise or column-wise, as long as each image is unfolded in the same way. In $\mathbf{X}$, temporal variation of each pixel is regarded as a variable, and SPCT extracts principal components (PCs) with linear combinations of these variables.

SPCT is an improvement of PCT [28], and the principles of PCT-based methods to extract features of the defects have been described in detail in the references [28], [29]. The feature extraction process of SPCT can be written as a regression-type optimization problem. The overall objective function is given as below [29], [43]

$$\widehat{\boldsymbol{P}}, \widehat{\boldsymbol{Q}} = \underset{\boldsymbol{P},\boldsymbol{Q}}{arg\,min} \left(\left\| \boldsymbol{X} - \boldsymbol{X}\boldsymbol{P}\boldsymbol{Q}^{\boldsymbol{T}} \right\|_{\boldsymbol{2}} + \delta \sum_{j=1}^{k} \left\| \boldsymbol{p}_j \right\|_{\boldsymbol{2}} + \lambda \sum_{j=1}^{k} \left\| \boldsymbol{p}_j \right\|_{\boldsymbol{1}} \right)$$
$$subject\ to\ \ \boldsymbol{Q}^{\boldsymbol{T}}\boldsymbol{Q} = \boldsymbol{I} \quad (16)$$

where $\mathbf{P} = [\mathbf{p}_1, \mathbf{p}_2, \ldots, \mathbf{p}_k]$ is the matrix formed by sparse loadings. In SPCT, sparse penalty constraints are introduced to the process of feature extraction, such that loadings of the variables with low level of variance will be sparse to 0. In (16), penalization terms of L1-norm ($\lambda \sum_{j=1}^{k} \left\| \mathbf{p}_j \right\|_1$) and L2-norm ($\delta \sum_{j=1}^{k} \left\| \mathbf{p}_j \right\|_2$) are added to the objective function.

Greedy research with an alternating algorithm can be applied to solve the optimization problem in (16). The detailed procedure is presented in the literature [43], which can be concluded as:

1. Initialize $\mathbf{Q}$ as the loadings of the first k ordinary principal components of $\mathbf{X}$.

2. Given $\mathbf{Q} = [\mathbf{q_1}, \mathbf{q_2}, \ldots, \mathbf{q_k}]$, solve the elastic net problem for $j = 1, 2, \ldots, k$ as below, with LARS-EN algorithm [44]

$$\widehat{\mathbf{p}}_\mathbf{j} = \arg\min_{\mathbf{P}_j} \left(\mathbf{q_j} - \mathbf{p_j}\right)^T \mathbf{X^T X} \left(\mathbf{q_j} - \mathbf{p_j}\right) + \delta \left\|\mathbf{p_j}\right\|^2 + \lambda \left\|\mathbf{p_j}\right\|_1 \tag{17}$$

3. For a fixed $\mathbf{P} = [\mathbf{p}_1, \mathbf{p}_2, \ldots, \mathbf{p}_k]$, compute the SVD of $\mathbf{X^T XP} = \mathbf{UDV^T}$, update $\mathbf{Q} = \mathbf{UV^T}$

4. Repeat 2-3 until convergence.

The most consuming step in the above process is to solve (17), with computational complexity of order $O(n^3)$, where n is the number of variables in $\mathbf{X}$. As for the case of extracting features from thermographic data, the number of characteristics $n = N_x N_y$, which is too large to boost the algorithm. To solve this problem, a soft-threshold algorithm [45], [46] is applied, replacing the elastic net problem in (17) with its special case ($\delta \to \infty$):

$$\widehat{\mathbf{p}}_\mathbf{j} = (\left|\mathbf{q_j^T X^T X}\right| - \frac{\lambda}{2})_+ Sign(\mathbf{q_j^T X^T X}) \tag{18}$$

In this alternative solution, complexity to compute (18) can be reduced to $O(n^2)$.

As a conclusion, the total procedures of DoGC-SPCT are summarized in Table 2. Furthermore, after conduction of the algorithm, a PC matrix $\mathbf{P}$ with dimension of $N_x N_y \times k$ is obtained. And then, each column vector can be further reshaped to a matrix with the size of $N_x \times N_y$, the same as that of the original thermogram. Therefore, a total of k feature maps can be formed and illustrated as pseudo-color images. Finally, inside those images, defective regions can be highlighted with different loading values compared to the intact regions.

IV. CASE STUDY

In this section, two CFRP specimens with artificial defects were investigated to validate the feasibility of the proposed DoGC-SPCT method. For comparison, some other feature extraction methods were also implemented for the thermographic data analysis.

To illustrate the effect of the methods more intuitively, the original thermal images and the extracted feature maps were demonstrated by means of pseudo-color images, with values of the entries converted to different colors.

Meanwhile, visualization of the defects can be quantitatively evaluated by the index of signal to noise ratio (SNR), which is described as [29], [30], [31]

$$SNR = \left|V_{def} - V_{in}\right| / \sigma_{in} \tag{19}$$

where V_{def} and V_{in} are the average values for the pixels inside defective and non-defective regions respectively, and σ_{in} is the standard deviation of the values in the non-defective region. In our research, the locations of those defects were identified depending on the priori knowledge about the specimen.

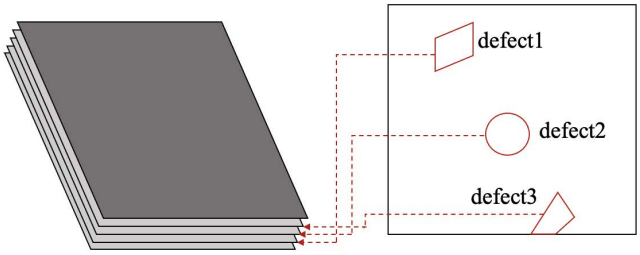

FIGURE 4. Distribution of the defects inside the CFRP specimen in Case1.

TABLE 2. The procedures of DoGC-SPCT.

Input: Original thermal images
Output: Feature maps of PCs
Procedures of the Algorithm:
Step1 Perform symmetric paddings and Gaussian convolutions with G_1 and G_2 kernels to each of the images.
Step2 Subtract G_2 convolutional result from that of G_1 convolution to obtain the smoothing result of the DoGC.
Step3 Vectorize the smoothed thermal images in row-wise to constitute a characteristic matrix $\mathbf{X}$. Decentralize $\mathbf{X}$ by subtracting the mean value from each variable to form matrix $\overline{\mathbf{X}}$.
Step4 Perform SPCT on $\overline{\mathbf{X}}$ to extract the sparse loadings $\mathbf{P}$.

A. CASE 1

1) INPUT DATASET

The thermographic data in the first case is the same as that in [29] and [34]. The original CFRP specimen corresponding to this data set is composed of 20 layers of carbon fiber sheets, and the manufacturing was carried out by a resin transfer molding process. At the same time, 3 subsurface defects were made manually by inserting flatly Teflon strips with different shapes during the manufacturing process. The detailed distributions of the defects inside the specimen are shown in Fig.4. According to the figure, the defects are numbered from 1 to 3 respectively to facilitate the following description. Among them, defect1 on the upper-left of the 2D plane lies beneath 3 layers of the sheets, defect2 locating in the middle is beneath 2 layers of the sheets, and defect3 on the lower-right of the 2D plane lies beneath 1 layer of the sheet.

For the conduction of PT, the specimen was stimulated by a 3000W flash lamp within 3ms. Meanwhile, the surface temperature of the specimen was captured by an infrared camera (TAS-G100EXD, NEC) during the cooling stage. The camera has a resolution of 320 × 240 and a sampling rate of 30 frames per second. The sampling process last for 3s, so that a total of 90 frames were recorded. In each sample, a sub-image containing 308 × 212 pixels was selected and analyzed in the following of this case.

2) RESULTS AND DISCUSSION

The parameters of DoGC in Case 1 were determined as described in 3.2.2. Considering the size of the dataset, the parameters are determined as Table 1. The analysis is conducted from 3 aspects: the performance of the DoGC filter,

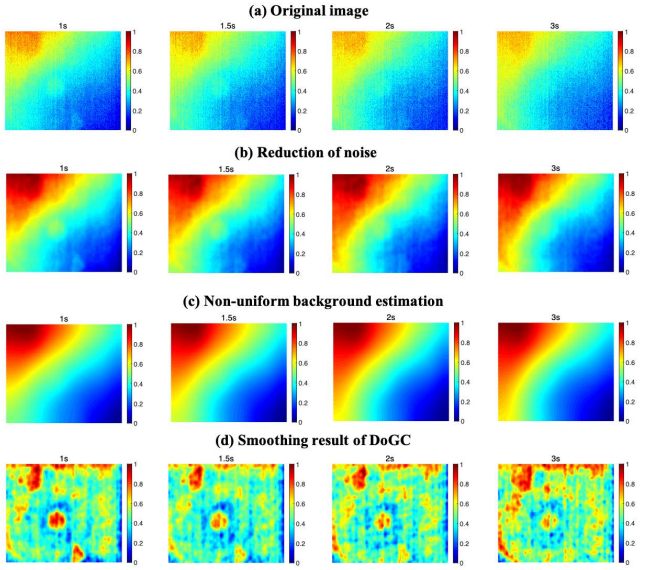

FIGURE 5. The results of the DoGC filter in Case1.

the features extracted by SPCT and finally the method comparison.

a: RESULTS OF DoGC FILTERING

Fig.5 illustrates the pseudo-color images of the smoothed results obtained by DoGC. For the sake of fairness, all the images before and after smoothing are normalized as below

$$\widehat{\mathrm{T}}\,(\mathrm{x},\mathrm{y},\mathrm{t}) = (\mathrm{T}\,(\mathrm{x},\mathrm{y},\mathrm{t}) - T_{t,min})/(T_{t,max} - T_{t,min}) \quad (20)$$

Fig.5(a) reveals the original images sampled at different time, where dynamic variations of the defects can be vaguely observed. With heat diffusing into the material, thermal contrast of the defects reaches its max value at about 1s, and then decreases gradually towards a steady state. On the other hand, the defect signals are seriously masked by noise and uneven background, making the defects difficult to be recognized. Fig.5(b) demonstrates the smoothed results of the first Gaussian convolutional filtering. Compared with Fig.5(a), most of the noise has been subtracted in Fig.5(b), and it is worth noticing that, the signals of the defects are retained after reduction of noise. Meanwhile, as visualized in Fig.5(c), non-uniform background is estimated by the second convolutional filtering, which is exclusive of defects and noise. Finally, Fig.5(d) shows the residual images obtained by subtracting the images in Fig.5(c) from those in Fig.5(b). Comparing Fig.5(d) and Fig.5(a), it can be seen that the defects can be further highlighted in the final results of DoGC filtering, with reduction of non-uniform background as well as noise. At the same time, as depicted in Fig.5(d), the temporal variation of the thermal contrasts for the defects is consistent with the process of heat diffusion, which is also revealed in Fig.5(a).

In order to quantitatively evaluate the results of filtering, normalized absolute contracts (NAC) of the defective regions and standard deviations of the sound regions are calculated.

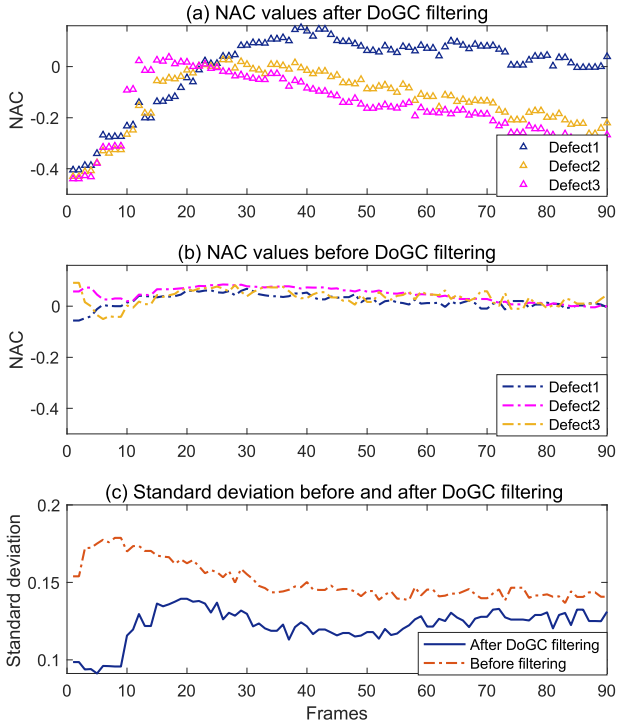

FIGURE 6. NACs for the defective regions and standard deviations for the sound regions.

The computation of NAC for image at time t is as below [27]:

$$\mathrm{NAC(t)} = \overline{\mathrm{T_d(t)}}/\overline{\mathrm{T_d(tmax)}} - \overline{\mathrm{T_n(t)}}/\overline{\mathrm{T_n(tmax)}} \quad (21)$$

where $\overline{\mathrm{T_d(t)}}$ and $\overline{\mathrm{T_n(t)}}$ represent the average values inside defective and non-defective regions respectively. Meanwhile, *tmax* is the time with maximum thermal contrast. According to (21), NAC is defined as the difference between the values of defective regions and non-defective regions. Also, it is a useful parameter to illustrate behaviors of thermal profiles.

Fig.6(a) and Fig.6(b) show the NAC values of the defects before and after DoGC filtering. As revealed in Fig.6(a), there are peaks occurring in the NAC curves obtained after DoGC filtering, meaning that the thermal contrast values of the defects go up and down in accordance with heat flow. In contrast, as for the original thermal images, NAC values for the defects keep around 0, reflecting that there is barely difference between defective and non-defective regions. The comparison of Fig.6(a) and Fig.6(b) illustrates that the DoGC filter helps to magnify the difference between defective regions and background, also it can enhance the temporal variation of thermal profiles for the defects. Therefore, the DoGC filtering makes the defective pixels more likely to be captured by the following feature extraction procedure.

Furthermore, Fig.6(c) demonstrates the standard deviation for the sound regions that reflects the smoothness of the background inside the thermal images. From Fig.6(c), it can be seen that after DoGC filtering, the standard deviation of the sound regions becomes smaller, indicating less interference in the filtering results. However, there are still errors left after filtering, leading to standard deviation larger than 0.

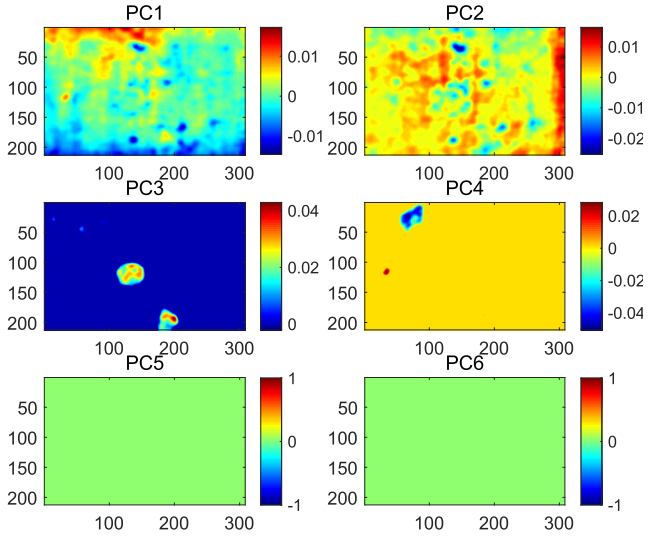

FIGURE 7. Feature extraction result of DoGC-SPCT in Case 1 ($\lambda = 800$).

As a conclusion of Fig.5 and Fig.6, the process of DoGC filtering can reduce noise and non-uniform background to a great extent, and thus it helps to amplify the difference between the values of defective and non-defective regions. In this way, the defective pixels can be more likely to be captured in the following feature extracting process.

b: RESULTS OF FEATURE EXTRACTION

The method of SPCT is then applied to extract features from the smoothed results of DoGC. Compared to other feature extraction methods, SPCT has the advantages of eliminating undesired features by setting their loadings as 0, so that it increases the interpretability of the result. In this paper, SPCT is performed according to the procedures presented in 3.3. In (16), the value of λ decides the level of sparsity during feature extraction, that is, with a higher λ, more features will be assigned as 0. However, there is not much guidance in justifying λ, because of the fact that detection situations may vary in different cases. We first set λ as 800 for an example, and the PCs extracted by SPCT are shown in Fig.7. This figure reveals that, the texture of the surface is captured in PC1 and PC2, while the three defects are extracted in PC3 and PC4 respectively. In this case, the defects are captured in separate PCs because they are located at different layers inside the specimen. Since defect1 lies in the deepest layer, it takes longer for heat flow to reach its location. Meanwhile, as depicted in Fig.6(a), the NAC curve of defect1 has a different variation pattern from those of defect2 and defect3. Consequently, features of defect1 are captured in a separate PC compared to the other defects. From this perspective, the order of PCs corresponding to different defects can help to discriminate the defects in accordance with their depths.

For a further discussion about values of λ, variations of PC3 and PC4 are plotted in Fig.8. λ is first set as 0, and the result in this situation is the same as that of PCT. As demonstrated in Fig.8, the pixels that are not related to

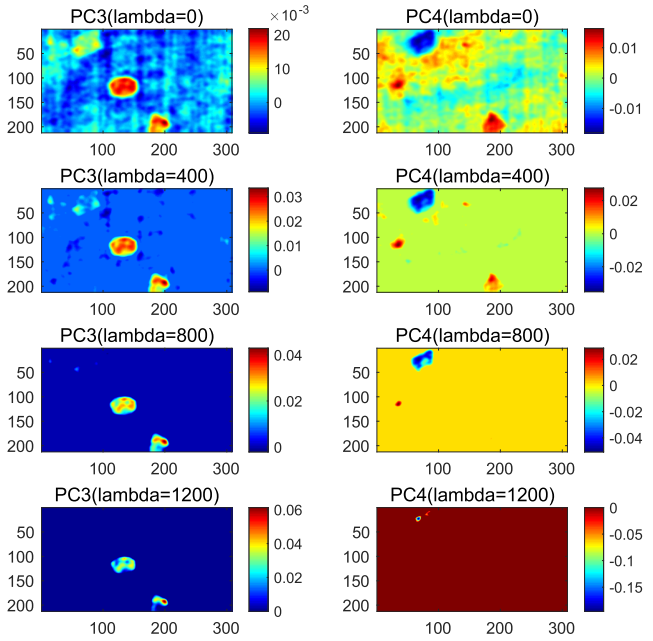

FIGURE 8. Variations of PC3 and PC4 against λ.

the defects are assigned with smaller loadings. Even though most of the interference can be eliminated through DoGC filtering, there are still tiny gaps between thermal profiles of the pixels. Therefore, without any sparsity, each pixel may be assigned with a separate value, and the unequal loadings make themselves like 'errors" in contrast with those of the defects. Furthermore, with the increasing of λ, more features for background are assigned as 0 through sparsity, leading to smoother background in the results. However, a higher level of sparsity will cause a distortion of the defect signals, as more pixels at boundary of the defects are sparse. Consequently, the identified defects will be smaller than their actual size. As shown in Fig.8, when λ is set as large as 1200, defect1 is almost eliminated with too high level of sparsity. Generally speaking, there is a balance between sparsity of the background and distortion of the defect signals, so that an appropriate value should be adjusted for λ. In this case, λ is set as 800 for the following study.

c: METHODS COMPARISON

To validate the feasibility of the proposed method, other feature extraction algorithms, including PCT, independent component thermography (ICT) [34], SPCT and GAN-SPCT [31] are also applied for comparisons. The extracted feature maps are visualized in Fig.9. And the SNRs of the defects are listed in Table 3. Meanwhile, SNRs from manually selected original frame with the most significant signals are also displayed to validate the effect of the methods.

Fig.9(a) and Fig.9(b) reveal the feature maps of PC3 and PC4 extracted by PCT, where the features of the defects are captured in sequence. As illustrated in the figures, PCT can enhance the visibility of the defects. Meanwhile, from Table 3, compared with original thermograms, higher SNR

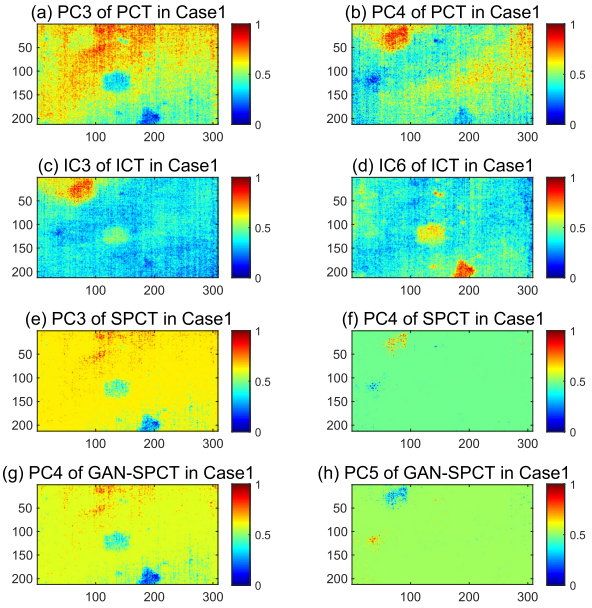

FIGURE 9. The features extracted by other methods in Case 1.

TABLE 3. SNRs of the defects in the results of different methods in Case 1.

Method	SNR (defect1)	SNR (defect2)	SNR (defect3)	λ
Original image	2.03	0.14	1.21	/
PCT	2.27	2.05	3.30	/
ICT	3.66	2.02	3.98	/
SPCT	3.54	2.72	6.34	2500
GAN-SPCT	5.13	2.73	6.28	2500
DoGC-SPCT	9.33	8.18	8.03	800

values are obtained by means of PCT. However, the enhancement by PCT is limited, as the results are contaminated by non-uniform background and noise.

Furthermore, Fig.9(c) and Fig.9(d) show the results of IC3 and IC6 obtained by ICT. According to [34], ICT is a signal separation method based on the principle of blind source separation. As shown in the figures, the defect signals can be separated from non-uniform background. However, the method of ICT can hardly separate noise from the defect signals. Therefore, the defects are relatively indistinct with rough background in the results of ICT.

Fig.9(e) and Fig.9(f) show the results obtained by SPCT. As shown in the figures, most of the loadings for the intact pixels in SPCT are sparse to 0, leading to more uniform background in the feature maps. Therefore, as illustrated in Table 3, SPCT obtains higher SNR values for the defects compared to PCT and ICT. However, since accuracy of feature extraction is affected by the interference of noise and background, some of the features for the defects are eliminated with sparsity. Consequently, the patterns of the defects, especially of defect1 are incomplete in the results.

Fig.9(g) and Fig.9(h) show the results obtained by GAN-SPCT, which is an improvement of SPCT with preprocess of data augmentation. According to ref [31], a deep convolutional GAN(DCGAN) model was constructed, and a total of 60 fake thermograms were generated. During feature extraction, λ with the same value of that in SPCT was applied for comparison. Revealed from the figures and Table 3, GAN-SPCT can enhance the effect of feature extraction to some extent. Theoretically, in GAN-SPCT, samples are expanded to enlarge the diversity of the original dataset, which facilitates identification of defects during feature extraction. However, GAN-SPCT is at risk of enhancing interference signals at the same time, as the diversity of the noise can also be magnified.

Finally, comparison of Fig.7 and Fig.9 reveals that the result obtained by DoGC-SPCT is outstanding among all these methods. Firstly, DoGC-SPCT further improves the visibility of the defects with obviously higher SNRs. As illustrated in Table 3, the relative increase rate as for SNR of defect2 by comparing DoGC-SPCT to SPCT can reach a maximum of 199.6%. Secondly, compared to SPCT and GAN-SPCT, DoGC-SPCT takes a much lower value of λ to obtain smoother background inside the feature maps, which increases the interpretability of the results. Compared with GAN-SPCT, DoGC-SPCT is also an improvement of SPCT, which proposes to eliminate noise and non-uniform background beforehand. In contrast to GAN-SPCT, DoGC-SPCT has a better performance in overcoming interference signals. Meanwhile, as aforementioned, after signal filtering, the DoGC filter enhances the thermal contrast of the defects in the resulting thermograms, so that it is more informative for defect identification and facilitates to eliminate features of the background.

B. CASE 2

1) INPUT DATASET

In order to validate the universality of the proposed method, a second test of CFRP specimen has been considered. For data acquisition in the second case, one specimen was detected by an experimental platform of pulsed thermography. The specimen in this case is composed of 6 carbon fiber sheets. And a total of 9 subsurface defects were made by embedding polytetrafluoroethylene (PTFE) of different shapes inside. Locations of the defects and the exterior of the specimen are shown in Fig.10. From the top view of the surface, the three defects on the right side are the shallowest, which lie beneath the first layer of the specimen. While the three defects in the middle are inserted beneath the third layer. Finally, the defects on the left side are the deepest, lying beneath the fifth layer of the specimen.

The experimental platform of pulsed thermography is shown in Fig.11.Two flash lamps with the highest power of 5KW are used as the excitation source. The IR camera is DALI© DL700, with the resolution of 640×480 and thermal sensitivity of 0.03°C. The sampling frequency of the camera

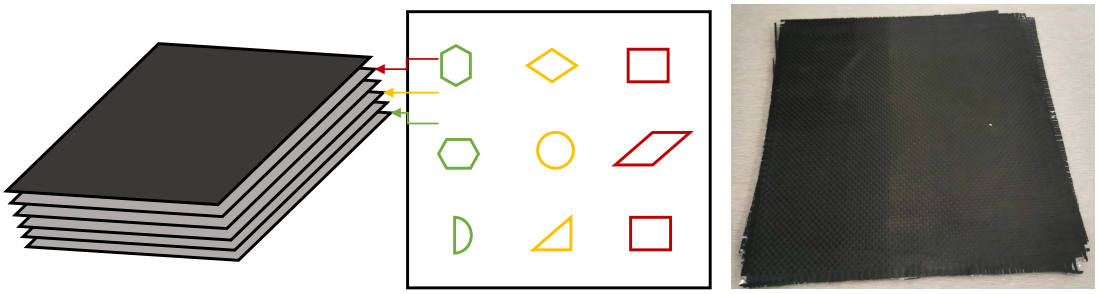

FIGURE 10. Locations of the defects and the exterior of the specimen in Case2.

FIGURE 11. The experimental platform of pulsed thermography in Case2.

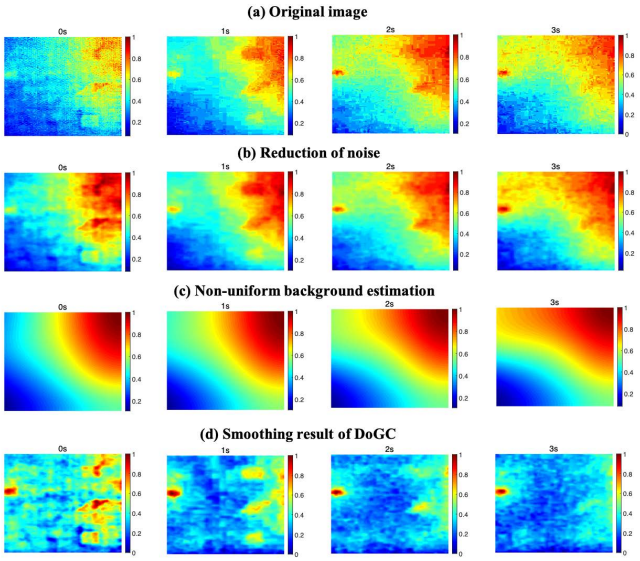

FIGURE 12. Effect of the DoGC filter in Case2.

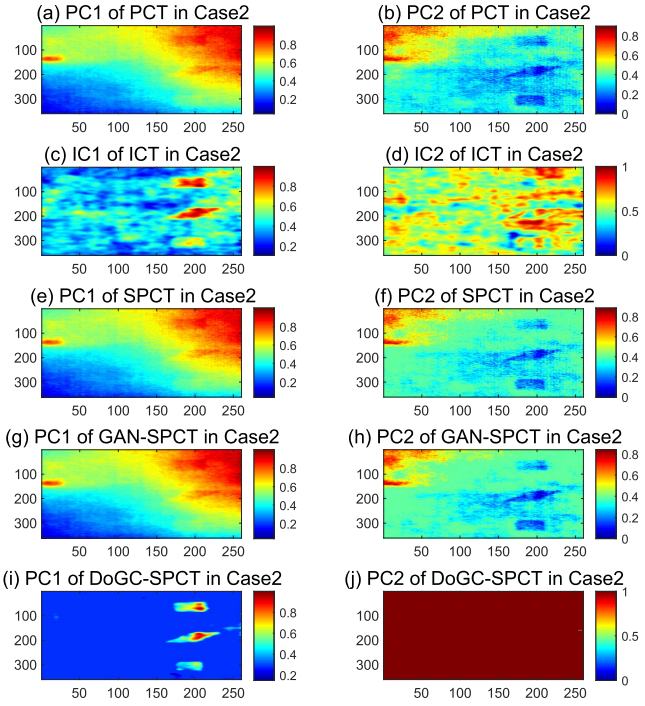

FIGURE 13. Feature extraction results by different methods in Case 2.

TABLE 4. SNRs of the defects in the results of different methods in Case 2.

Method	SNR (defect1)	SNR (defect2)	SNR (defect3)	λ
Original image	1.75	1.20	0.23	/
PCT	1.20	1.69	1.63	/
ICT	3.72	3.16	1.99	/
SPCT	1.22	1.92	1.83	10000
GAN-SPCT	1.25	2.03	1.93	25000
DoGC-SPCT	8.82	7.14	4.10	7000

is 6 frames per second, and a total of 40 frames of thermal images were recorded. For data analysis, original images are cropped to sub-images with the size of 270 × 360.

2) RESULTS AND DISCUSSION

Parameters of DoGC-SPCT in Case 2 are justified as in Table 1. The effects of DoGC are demonstrated in Fig.12. From this figure, it can be seen that, the shallowest 3 defects can be vaguely observed in the original thermograms, and attenuation of heat makes those deeper defects invisible. What needs to be emphasized is that, the bright speck on the left is caused by the reflection of the light source rather than the defects. As depicted in Fig.12, the DoGC filtering can reduce noise and background from the original images, thus it can magnify the thermal difference between the defective regions and intact regions.

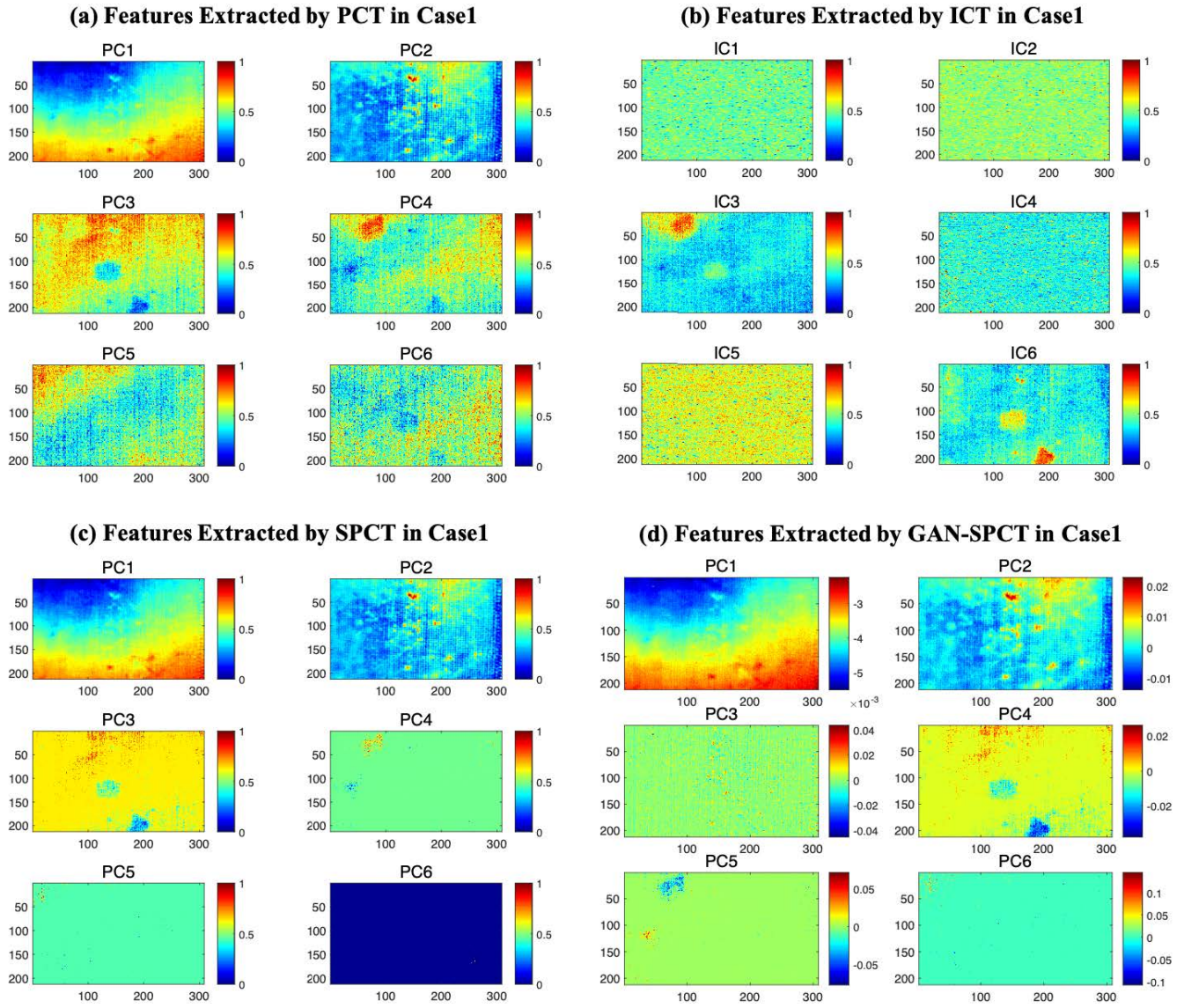

FIGURE 14. Features extraction by different methods in Case1.

The methods of PCT, ICT, SPCT, GAN-SPCT are also compared to validate the feasibility of DoGC-SPCT. Fig.13 and Table 4 demonstrate the extracted features and the SNR results respectively. In Table 4, since the original SNR for defect1 is affected by the uneven temperature distribution, it leads to a higher value compared to those in PCT, SPCT and GAN-SPCT. The same with Case 1, DoGC-SPCT is superior to the other methods in overcoming the interference from noise and non-uniform background. As a result, DoGC-SPCT can increase the SNR values for the defects significantly. Meanwhile, a much lower value of λ is needed in DoGC-SPCT to smooth the background, so that DoGC-SPCT shows higher interpretability in the results.

V. CONCLUSION

This paper presented a novel feature extraction method named as DoGC-SPCT to deal with thermographic data. In this method, a DoGC filter is proposed to subtract noise and non-uniform background as preprocessing. Thus, it can highlight the temporal variations in the thermal profiles of defective pixels and facilitate identification of defects in the feature extraction. The experimental results demonstrated that, the DoGC filter can reduce most of the noise and non-uniform background signals, so that the difference between defective and non-defective regions can be increased in the smoothed results. Compared to the common feature extracting methods, DoGC-SPCT is superior in increasing the SNR values for the defects. And it can increase the interpretability of the results with more uniform background.

This paper has verified the effectiveness of DoGC-SPCT. Future work will focus on increasing the accuracy of this methodology, so that automatic recognition as well as quantitative analysis of defects can be conducted.

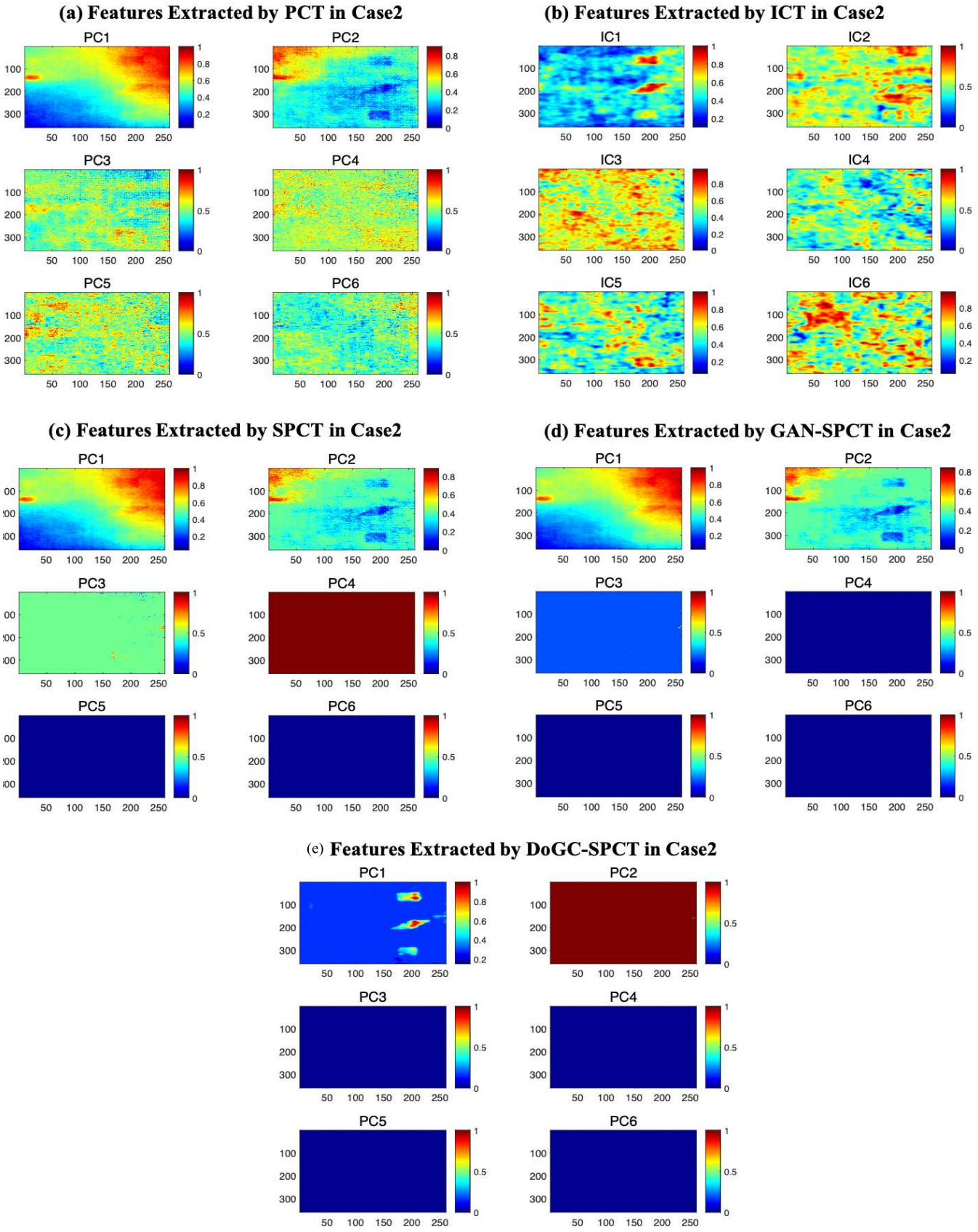

FIGURE 15. Features extraction by different methods in Case2.

APPENDIX

The first 6 components obtained from the methods in Case1 of our study is shown in Fig. 14. And the first 6 components obtained from the methods in Case2 of our study is shown in Fig. 15.

REFERENCES

[1] J. Xie, Z. Lu, Y. Guo, and Y. Huang, "Durability of CFRP sheets and epoxy resin exposed to natural hygrothermal or cyclic wet-dry environment," *Polym. Compos.*, vol. 40, no. 2, pp. 553–567, Feb. 2019.

[2] J. Vorderbrüggen and G. Meschut, "Investigations on a material-specific joining technology for CFRP hybrid joints along the automotive process chain," *Compos. Struct.*, vol. 230, Dec. 2019, Art. no. 111533.

[3] S. D. P. D. Ammbrois, I. Corazzari, O. Damiano, L. Cornillon, A. Terenzi, V. Casalegno, and M. Ferraris, "Adhesive joining of Zerodur–CFRP–Zerodur sandwich structures for aerospace applications," *Macromol. Mater. Eng.*, vol. 305, no. 12, Dec. 2020, Art. no. 2000464.

[4] K. Nakahata, K. Ogi, K. Mizukami, K. Ohira, M. Maruyama, S. Wada, T. Namita, and T. Shiina, "Three-dimensional imaging of subsurface delamination in carbon fiber reinforced plastic using photoacoustic wave method," *Electron. Commun. Jpn.*, vol. 102, no. 5, pp. 35–42, May 2019.

[5] Y. Chen, X. Guo, K. Zhang, D. Guo, C. Zhou, and L. Gai, "Study on the surface quality of CFRP machined by micro-textured milling tools," *J. Manuf. Processes*, vol. 37, pp. 114–123, Jan. 2019.

[6] Z. Li, A. Haigh, C. Soutis, A. Gibson, and P. Wang, "A review of microwave testing of glass fibre-reinforced polymer composites," *Nondestruct. Test. Eval.*, vol. 34, no. 4, pp. 429–458, Apr. 2019.

[7] E. Dilonardo, M. Nacucchi, F. De Pascalis, M. Zarrelli, and C. Giannini, "High resolution X-ray computed tomography: A versatile non-destructive tool to characterize CFRP-based aircraft composite elements," *Compos. Sci. Technol.*, vol. 192, May 2020, Art. no. 108093.

[8] B. Salski, W. Gwarek, P. Korpas, S. Reszewicz, A. Y. B. Chong, P. Theodorakeas, I. Hatziioannidis, V. Kappatos, C. Selcuk, T.-H. Gan, M. Koui, M. Iwanowski, and B. Zielinski, "Non-destructive testing of carbon-fibre-reinforced polymer materials with a radio-frequency inductive sensor," *Compos. Struct.*, vol. 122, pp. 104–112, Apr. 2015.

[9] V. Dattoma, F. W. Panella, A. Pirinu, and A. Saponaro, "Ultrasonic and thermographic studies for CFRP inspections with real and simulated defects," *Mater. Today, Proc.*, vol. 34, pp. 224–234, Jan. 2021.

[10] N. Toyama, T. Yamamoto, K. Urabe, and H. Tsuda, "Ultrasonic inspection of adhesively bonded CFRP/aluminum joints using pulsed laser scanning," *Adv. Compos. Mater.*, vol. 28, no. 1, pp. 27–35, Jan. 2019.

[11] A. N. Abdalla, M. A. Faraj, F. Samsuri, D. Rifai, K. Ali, and Y. Al-Douri, "Challenges in improving the performance of eddy current testing: Review," *Meas. Control*, vol. 52, nos. 1–2, pp. 46–64, Nov. 2018.

[12] Q. Feng, B. Gao, P. Lu, W. L. Woo, Y. Yang, Y. Fan, X. Qiu, and L. Gu, "Automatic seeded region growing for thermography debonding detection of CFRP," *NDT E Int.*, vol. 99, pp. 36–49, Oct. 2018.

[13] A. D. Restrepo-Girón and H. Loaiza-Correa, "Background thermal compensation by filtering for contrast enhancement in active thermography," *J. Nondestruct. Eval.*, vol. 35, no. 1, pp. 1–11, Mar. 2016.

[14] R. Marani, D. Palumbo, U. Galietti, E. Stella, and T. D'Orazio, "Enhancing defects characterization in pulsed thermography by noise reduction," *NDT E Int.*, vol. 102, pp. 226–233, Mar. 2019.

[15] X. Zhang, J. Saniie, and A. Heifetz, "Spatial temporal denoised thermal source separation in images of compact pulsed thermography system for qualification of additively manufactured metals," in *Proc. IEEE Int. Conf. Electro Inf. Technol. (EIT)*, May 2021, pp. 209–214.

[16] F. W. Panella and A. Pirinu, "Application of pulsed thermography and post-processing techniques for CFRP industrial components," *J. Nondestruct. Eval.*, vol. 40, no. 2, pp. 1–17, Jun. 2021.

[17] W. F. Da Silva, R. A. C. Melo, M. Grosso, G. R. Pereira, and D. B. Riffel, "Active thermography data-processing algorithm for nondestructive testing of materials," *IEEE Access*, vol. 8, pp. 175054–175062, 2020.

[18] X. Zhang, J. Saniie, S. Bakhtiari, and A. Heifetz, "Compression of pulsed infrared thermography data with unsupervised learning for nondestructive evaluation of additively manufactured metals," *IEEE Access*, vol. 10, pp. 9094–9107, 2022.

[19] E. D'Accardi, D. Palumbo, R. Tamborrino, and U. Galietti, "A quantitative comparison among different algorithms for defects detection on aluminum with the pulsed thermography technique," *Metals*, vol. 8, no. 10, p. 859, Oct. 2018.

[20] Y. Chung, S. Lee, and W. Kim, "Latest advances in common signal processing of pulsed thermography for enhanced detectability: A review," *Appl. Sci.*, vol. 11, no. 24, p. 12168, Dec. 2021.

[21] Y. Liu, M. Zheng, K. Liu, Y. Yao, and S. Sfarra, "TriMap thermography with convolutional autoencoder for enhanced defect detection of polymer composites," *J. Appl. Phys.*, vol. 131, no. 14, Apr. 2022, Art. no. 144901.

[22] X. Zhang, J. Saniie, and A. Heifetz, "Neural learning based blind source separation for detection of material defects in pulsed thermography images," in *Proc. IEEE Int. Conf. Electro Inf. Technol. (EIT)*, May 2020, pp. 112–116.

[23] N. Saeed, Y. Abdulrahman, S. Amer, and M. A. Omar, "Experimentally validated defect depth estimation using artificial neural network in pulsed thermography," *Infr. Phys. Technol.*, vol. 98, pp. 192–200, May 2019.

[24] R. Marani, D. Palumbo, U. Galietti, and T. D'Orazio, "Deep learning for defect characterization in composite laminates inspected by step-heating thermography," *Opt. Lasers Eng.*, vol. 145, Oct. 2021, Art. no. 106679.

[25] A. I. Moskovchenko, V. P. Vavilov, R. Bernegger, C. Maierhofer, and A. O. Chulkov, "Detecting delaminations in semitransparent glass fiber composite by using pulsed infrared thermography," *J. Nondestruct. Eval.*, vol. 39, no. 3, pp. 1–10, Sep. 2020.

[26] U. Netzelmann and D. Müller, "Modified pulse-phase thermography algorithms for improved contrast-to-noise ratio from pulse-excited thermographic sequences," *NDT E Int.*, vol. 116, Dec. 2020, Art. no. 102325.

[27] C. A. Alvarez-Restrepo, H. D. Benitez-Restrepo, and L. E. Tobón, "Characterization of defects of pulsed thermography inspections by orthogonal polynomial decomposition," *NDT E Int.*, vol. 91, pp. 9–21, Oct. 2017.

[28] N. Rajic, "Principal component thermography for flaw contrast enhancement and flaw depth characterisation in composite structures," *Compos. Struct.*, vol. 58, pp. 521–528, Dec. 2002.

[29] J.-Y. Wu, S. Sfarra, and Y. Yao, "Sparse principal component thermography for subsurface defect detection in composite products," *IEEE Trans. Ind. Informat.*, vol. 14, no. 12, pp. 5594–5600, Dec. 2018.

[30] K. Liu, Y. Li, J. Yang, Y. Liu, and Y. Yao, "Generative principal component thermography for enhanced defect detection and analysis," *IEEE Trans. Instrum. Meas.*, vol. 69, no. 10, pp. 8261–8269, Oct. 2020.

[31] W. Liu, B. Hou, Y. Wang, Y. Yao, and L. Zhou, "Sparse structural principal component thermography for defect signal enhancement in subsurface defects detection of composite materials," *J. Nondestruct. Eval.*, vol. 41, no. 1, pp. 1–17, Dec. 2021.

[32] S. Grys, "New thermal contrast definition for defect characterization by active thermography," *Measurement*, vol. 45, no. 7, pp. 1885–1892, Aug. 2012.

[33] K. Zheng, Y.-S. Chang, and Y. Yao, "Defect detection in CFRP structures using pulsed thermographic data enhanced by penalized least squares methods," *Compos. B, Eng.*, vol. 79, pp. 351–358, Sep. 2015.

[34] Y. Liu, J.-Y. Wu, K. Liu, H.-L. Wen, Y. Yao, S. Sfarra, and C. Zhao, "Independent component thermography for non-destructive testing of defects in polymer composites," *Meas. Sci. Technol.*, vol. 30, no. 4, Mar. 2019, Art. no. 044006.

[35] H. Wang, M. Wang, J. Li, L. Song, and Y. Hao, "A novel signal separation method based on improved sparse non-negative matrix factorization," *Entropy*, vol. 21, no. 5, p. 445, Apr. 2019.

[36] M. Esteki, Z. Shahsavari, and J. Simal-Gandara, "Use of spectroscopic methods in combination with linear discriminant analysis for authentication of food products," *Food Control*, vol. 91, pp. 100–112, Sep. 2018.

[37] W. Liu, Y. Zhang, L. Zhou, and Y. Lyu, "Difference of Gaussian convolutional sparse principal component thermography for defect signal enhance in composite materials," in *Proc. 3rd Int. Conf. Ind. Artif. Intell. (IAI)*, Nov. 2021, pp. 1–5.

[38] A. I. Zhmakin, "Heat conduction beyond the Fourier law," *Tech. Phys.*, vol. 66, no. 1, pp. 1–22, Feb. 2021.

[39] Y.-S. Chang, Z. Yan, K.-H. Wang, and Y. Yao, "Non-destructive testing of CFRP using pulsed thermography and multi-dimensional ensemble empirical mode decomposition," *J. Taiwan Inst. Chem. Eng.*, vol. 61, pp. 54–63, Apr. 2016.

[40] J. Wu, S. Zhang, Z. Xiao, F. Zhang, L. Geng, S. Lou, and M. Liu, "Hemorrhage detection in fundus image based on 2D Gaussian fitting and human visual characteristics," *Opt. Laser Technol.*, vol. 110, pp. 69–77, Feb. 2019.

[41] S. S. Nidhyanandhan, R. Sindhuja, and R. S. S. Kumari, "Double stage Gaussian filter for better underwater image enhancement," *Wireless Pers. Commun.*, vol. 114, no. 4, pp. 2909–2921, Oct. 2020.

[42] S. Wu, G. Wang, P. Tang, F. Chen, and L. Shi, "Convolution with even-sized kernels and symmetric padding," in *Proc. Adv. Neural Inf. Process. Syst. (NIPS)*, vol. 32, 2019, pp. 1–12.
[43] H. Zou and L. Xue, "A selective overview of sparse principal component analysis," *Proc. IEEE*, vol. 106, no. 8, pp. 1311–1320, Aug. 2018.
[44] M. N. Tabassum and E. Ollila, "Pathwise least angle regression and a significance test for the elastic net," in *Proc. 25th Eur. Signal Process. Conf. (EUSIPCO)*, Aug. 2017, pp. 1309–1313.
[45] T. Zhu, "A convergence analysis for iterative sparsification projection with soft-thresholding," *Signal, Image Video Process.*, vol. 15, no. 8, pp. 1705–1712, Nov. 2021.
[46] L. Zhou, J. Zheng, Z. Ge, Z. Song, and S. Shan, "Multimode process monitoring based on switching autoregressive dynamic latent variable model," *IEEE Trans. Ind. Electron.*, vol. 65, no. 10, pp. 8184–8194, Oct. 2018.

WEI LIU received the B.S. and Ph.D. degrees in controling science and engineering from the Department of Control Science and Engineering, Zhejiang University, in 2013 and 2019, respectively. She is currently working as a Lecturer with the School of Automation and Electrical Engineering, Zhejiang University of Science & Technology. Her research interests include nondestructive detection, artificial intelligent, and big data analysis.

BEIPING HOU received the Ph.D. degree in controling science and engineering from Zhejiang University, in 2005. He is currently a Professor at the School of Automation and Electrical Engineering, Zhejiang University of Science & Technology, Hangzhou, China. His current research interests include machine vision, pattern recognition, and automatic control.

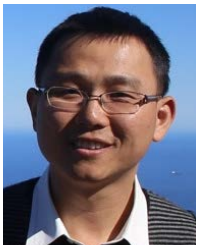

YUAN YAO (Member, IEEE) received the bachelor's and master's degrees in controling science and engineering from Zhejiang University, Hangzhou, China, in 2001 and 2004, respectively, and the Ph.D. degree in chemical and biomolecular engineering from the Hong Kong University of Science and Technology (HKUST), Hong Kong, in 2009.

From 2009 to 2011, he was a Research Associate with the Center for Polymer Processing and Systems, HKUST. From 2011 to 2015, he was an Assistant Professor with the Department of Chemical Engineering, National Tsing Hua University, Hsinchu, Taiwan. After that, he was an Associate Professor with the Department of Chemical Engineering, from 2015 to 2019. Since August 2019, he has been a Full Professor with the Department of Chemical Engineering. He is the author of 98 SCI journal articles, two book chapter, and nine patents. His research interests include process data analytics, process monitoring, soft sensor techniques, nondestructive testing data processing, and process control.

LE ZHOU (Member, IEEE) received the B.Eng. and Ph.D. degrees from the Department of Control Science and Engineering, Zhejiang University, Hangzhou, China, in 2010 and 2015, respectively. He was a Visiting Scholar with the Viterbi School of Engineering, University of Southern California, Los Angeles, CA, USA, from December 2013 to June 2014, and a Visiting Scholar with the Department of Chemical Engineering, Chung Yuan Christian University, Chung-Li, Taoyuan, Taiwan, from November 2014 to January 2015. He is currently an Associate Professor with the School of Automation and Electrical Engineering, Zhejiang University of Science & Technology. His research interests include industrial process modeling, monitoring and fault diagnosis, soft sensor modeling, and deep learning.